Inorganic Chemistry

ARTICLE

pubs.acs.org/IC

Controlled Fabrication and Shape-Dependent Luminescence Properties of Hexagonal $NaCeF_4$, $NaCeF_4$:Tb^{3+} Nanorods via Polyol-Mediated Solvothermal Route

Xuesong Qu,[†,‡] Hyun Kyoung Yang,[†] Guohui Pan,[§] Jong Won Chung,[†] Byung Kee Moon,[†] Byung Chun Choi,[†] and Jung Hyun Jeong*[,†]

[†]Department of Physics, Pukyong National University, Korea Busan 608-737, South Korea

[‡]Department of Physics, Changchun Normal University, Changchun 130032, China

[§]Institut de Recherche Interdisciplinaire (IRI, USR-3078), Parc de la Haute Borne, 50 Avenue de Halley, BP 70478, 59658 Villeneuve d'Ascq, France

Supporting Information

ABSTRACT: Hexagonal monodisperse $NaCeF_4$ and $NaCeF_4$:Tb^{3+} nanorods have been successfully synthesized by a polyol-mediated solvothermal route with ethylene glycol (EG) as solvent. The crystalline phase, size, morphology, and luminescence properties were characterized using X-ray diffraction (XRD), scanning electron microscopy (SEM), transmission electron microscopy (TEM), and photoluminescence (PL) spectra as well as dynamic decays. The experimental results indicate that the content of NH_4F and $NaNO_3$ are crucial in controlling product morphology and size. Nanorods with different aspect ratios could be controllably obtained under settled conditions. Shape-dependent luminescence and energy transfer routes from Ce^{3+} to Tb^{3+} in $NaCeF_4$:Tb^{3+} nanorods were observed by the modified local crystal field environment around rare earth ions. The 4f−5d transitions of Ce^{3+} ions have much higher sensitivity to the anisotropic shape of samples than that of Tb^{3+} ions.

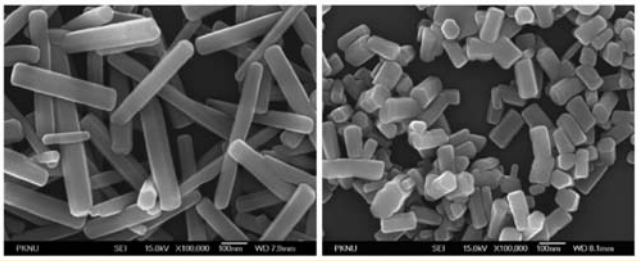

1. INTRODUCTION

Recently, much more attention has been focused on the shape and size-controlled synthesis of luminescent nanomaterials based on rare earth (RE) ions due to their size/shape-dependent properties and many promising applications in optics,[1] optoelectronics, biological labeling,[2] light emitting devices,[3] etc. It is expected that the physical and chemical properties of nanocrystals could be manipulated as desired by precisely controlling the size and morphologies.[4] Therefore, the controlled fabrication of rare-earth doped luminescent nanocrytals represents a great challenge and is of fundamental and technical importance.

Among various host materials for RE ions, RE fluorides possess advantageous properties over the oxygen-based systems as a fluorescent host matrix, resulting from their low vibration energy and, thus, subsequent minimization for the quenching of the excited state of the RE ions.[5−8] Particularly, fluorides based on an $ALnF_4$ (A = alkaline metal, Ln = RE element) system with unique luminescent, ferromagnetic, insulating/magnetic, and piezoelectric properties have drawn particular attention because of their wide applications as solid electrolytes, solid-state lasers, and up- or down-conversion hosts.[9,10] Dramatic efforts have been dedicated to its design and synthesis of controlled morphologies and size.[11−18] Up to the present, $ALnF_4$ nanocrystals have been prepared through various wet chemical routes such as solid treatment,[8] coprecipitation,[2] hydrothermal method,[10−12] liquid−solid-solution (LSS) procedure,[13,14] solvothermal methods,[15] and so forth. In particular, the organometallic and its alternatives are relatively successful synthetic methods. Through the cothermolysis of $Na(CF_3COO)$ and $RE(CF_3COO)_3$ in high-boiling solvent of oleic acid/oleylamine, a high quality of $NaREF_4$ (RE: Pr to Lu, Y) nanocrystals (nanorods, nanoplates, nanospheres, nanopolyhedra) have been synthesized by Mai et al.[15] With the liquid−solid two phase approach, Chen's group[16] got the oil-dispersible $NaYF_4$ nanoplates. A more recent hydrothermal method using oleic acid as stabilizing agent yielded shape, size, and phase-controlled synthesis of α-$NaREF_4$ (RE: Dy, Ho, Er, Tm, Y, Yb, and Lu) and β-$NaREF_4$ (RE: Pr to Lu, Y). However, the aforementioned wet chemical routes to the $NaREF_4$ system were limited to those RE cations with small radius. Reports on early lanthanide ions in the system of $NaREF_4$ (RE: La−Ce) nanocrystals are still rare. In the hexagonal β-$NaREF_4$ series, it is known that lattice constants show a systematic variation from 6.157 to 5.967 Å for a_0 and from

Received: November 9, 2010
Published: March 15, 2011

3.822 to 3.528 Å for c_0 with the sequential decreases of cation radius from La^{3+} (1.06 Å) to Lu^{3+} (0.85 Å). As a consequence, it seems somewhat difficult to settle the cations into the lattice to get the crystalline compounds with large rare earth cations such as $NaNdF_4$, $NaPrF_4$, and $NaCeF_4$. Until recently, $NaPrF_4$ and $NaNdF_4$ nanocrystals were prepared by Mai et al. in high-boiling organic solvent at much higher temperature (330 °C) using toxic precursors.[15] Zeng's et al. studies[17] showed that the $NaCeF_4$ could be prepared by a solvothermal method and that basic solution seemed to favor its formation. However, no detailed reactant receipts and synthesis procedures were described. In this work, we reported a controlled synthesis of size-tunable monodisperse $NaCeF_4$ nanorods via a facile polyol method. The effects of the content of NH_4F and $NaNO_3$ on the morphology and size of the final products were studied in detail. The photoluminescent (PL) properties of Tb^{3+} doped $NaCeF_4$ samples were also investigated.

2. EXPERIMENTAL SECTION

2.1. Sample Preparation. All chemicals were of analytical grade and were used as received without further purification. In a typical procedure for the preparation of $NaCeF_4$ nanocrystals, 32 mmol of NH_4F was dissolved in 20 mL of ethylene glycol (EG). Afterward, a solution of 2 mmol of $Ce(NO_3)_3 \cdot 6H_2O$ and 2 mmol of $NaNO_3$ in 20 mL of EG was added into the above solution under vigorous stirring. After stirring for 30 min, the mixed solution was transferred into a Teflon bottle of 70 mL held in a stainless steel autoclave, sealed, and maintained at 180 °C for 48 h. As the autoclave was cooled to room temperature naturally, the precipitates were separated by centrifugation, washed with deionized water and ethanol in sequence, and then dried in air at 70 °C for 12 h. Different NH_4F content (16, 18, 20, 24, 28, 32, 48, and 60 mmol) and different $NaNO_3$ content (2, 3, 4, 6, 8, and 10 mmol) were selected to study the effects on the morphology and size of the products. It should be pointed out that, when the effect of one reaction condition was studied, the other reaction conditions were kept the same as those for the typical synthesis. $NaCeF_4$:Tb^{3+} (10 mol %) nanocrystals were prepared in the same procedures except for adding 1.8 mmol of $Ce(NO_3)_3 \cdot 6H_2O$ and 0.2 mmol of $Tb(NO_3)_3 \cdot 6H_2O$ instead of 2 mmol of $Ce(NO_3)_3 \cdot 6H_2O$.

2.2. Measurements and Characterization. X-ray diffraction (XRD) patterns of the samples were obtained with a Philips XPert/MPD diffraction system with Cu Kα radiation (λ = 1.54056 Å). Field emission scanning electron micrograph (FESEM) images were taken on a Hitachi S-4200 electron microscope. A transmission electron micrograph and selective area electron diffraction patterns (SAED) were obtained on a JEM-2010 JEOL electron microscope using an accelerating voltage of 200 kV. The visible emissions were collected using a PTI (Photon Technology International) fluorimeter using a Xe-arc lamp with a power of 60 W. The lifetimes were measured using a phosphorimeter attachment to the main system with a Xe-flash lamp (25 W power) with a dominant excitation wavelength of 245 nm.

3. RESULTS AND DISCUSSION

As it is well-known, crystal morphology depends not only on the intrinsic crystal structure of the target compounds but also on the growth surroundings.[6,19] Many works indicated that successful fabrication of high quality nanocystals in a solution-based system also requires more fastidious control on the growth parameters such as reaction temperature, time, pH value of the precursor solution, organic additives, and so forth.[20] In this work,

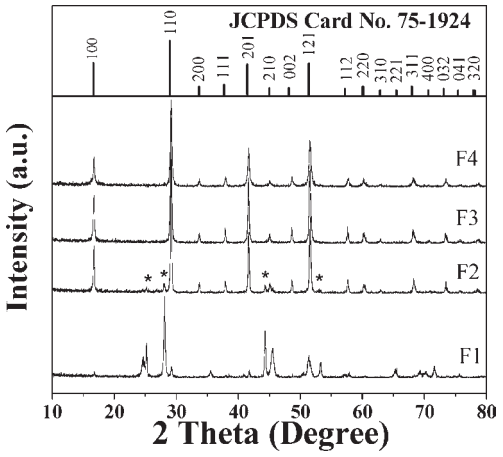

Figure 1. XRD patterns of as-prepared samples synthesized with different NH_4F content of 18, 24, 32, and 48 mmol, respectively, and fixed amounts of Ce and Na sources in 20 mL of EG. Pure hexagonal $NaCeF_4$ (JCPDS No. 75-1924, topmost line spectrum) can be obtained under the condition of 32 mmol of NH_4F or more, 2 mmol of $NaNO_3$, and 2 mmol of $Ce(NO_3)_3$ in 20 mL of EG. Diffraction peaks from CeF_3 phase were denoted as an asterisk in the mixture.

we mainly focused on the effects of reactant content of $NaNO_3$ and NH_4F on morphology of the final $NaCeF_4$ nanocrystals.

3.1. Effect of NH_4F Content. In this paper, NH_4F was used as the F source for the preparation of $NaCeF_4$ nanocrystals. Different NH_4F contents of 16, 18, 20, 24, 28, 32, 48, and 60 mmol were selected to study the production of hexagonal $NaCeF_4$; that is, in all the experiments, the F source is excessive with regard to the fixed amounts of Ce and Na sources (2 mmol). In particular, the samples synthesized with NH_4F content of 18, 24, 32, 48, and 60 mmol were selectively referred to as F1, F2, F3, F4, and F5, respectively, for other demonstration. Figure 1 shows XRD patterns of as-obtained samples mentioned above and the standard data for $NaCeF_4$. The results indicate that the NH_4F content plays an important role in the formation process of $NaCeF_4$. In the case of sample which is synthesized with NH_4F content of 16 mmol, $NaCeF_4$ could not be prepared, but a combination of hexagonal CeF_3 (JCPDS Card No. 08-0045) and cubic phase CeF_2 (JCPDS Card No. 34-0672) was obtained instead (see Figure S1(A), Supporting Information). It should be noted that the amount of 16 mmol used in this experiment has doubled the chemically stoichiometric value. When the NH_4F content approached 18 mmol, hexagonal phase $NaCeF_4$ rods started to form; however, a small quantity of hexagonal CeF_3 could still be detected at the NH_4F content of 24 and 28 mmol, respectively. Pure $NaCeF_4$ rods were not successfully obtained until increasing the NH_4F to 32 mmol, where all the reflection peaks of samples can be indexed to a hexagonal phase structure (JCPDS No. 75-1924, topmost line spectrum). Upon further increasing the content of NH_4F to 32 and 60 mmol, pure hexagonal phase $NaCeF_4$ was still prepared. The recent demonstrations[21,22] show that hexagonal sodium yttrium fluoride is of the $Na_{3x}M_{2-x}F_6$ type structure with M═La−Sm (with space group $P6_3/m$, $Z = 1$) and the crystal structure consists of an ordered array of F^- ions with two types of partially ordered cation sites selectively occupied by Na^+ and RE^{3+} ions; that is, the ($1/3RE^{3+}$, $1/3Na^+$) ions occupy sites with the 9-fold tricapped trigonal prism coordination, while the remaining sodium ions occupy sites with the 6-fold octahedral coordination

dx.doi.org/10.1021/ic1022467 |Inorg. Chem. 2011, 50, 3387–3393

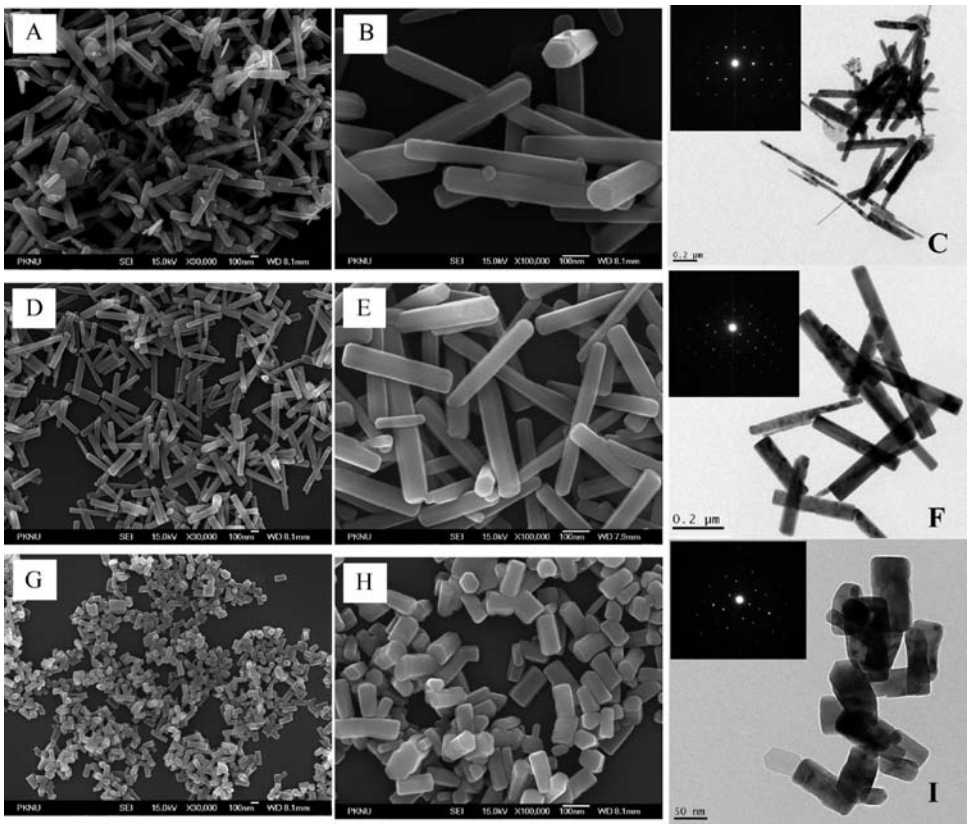

Figure 2. FE-SEM and TEM images of $NaCeF_4$ samples. (A−C): F2; (D−F): F3; (G−I) F4. The inset in the TEM images are SAED patterns from a single nanorod.

(cf. Figures 4 and 1b in refs 21 and 22, respectively). In terms of the slightly smaller ion radius of Tb^{3+} (r = 1.095 Å)[23] compared with Ce^{3+} (r = 1.196 Å),[23] incorporation of Tb^{3+} may induce unit cell shrinking and change the local symmetry slightly.

The morphology of the as-prepared samples F2−5 was illustrated in Figures 2 and S2(A,B), Supporting Information. It can be seen that all three $NaCeF_4$ products consist of nearly uniform hexagonal nanorods. The average diameters are about 110, 100, 100, and 80 nm, and the average lengths are about 700, 500, 150, and 100 nm, corresponding to samples F2, F3, F4, and F5, respectively. That is, the length of nanorods decreased systematically from F2 to F5; however, the diameter changed only a little. Transmission electron microscopy (TEM) images of the three samples (F2−F4) further verify the size and shape of nanorods; more importantly, regularly arranging diffraction spots in the pattern of SAED from a single nanorod indicates their single crystalline nature. The higher the NH_4F content, the smaller was the obtained aspect ratio L/D (length/diameter). This result demonstrates that the NH_4F content has a great influence on the morphology of products. As well documented in the literature, aspect ratio could be mechanistically determined by the relative rates of growth along different crystallographic directions. In general, faces perpendicular to the fast directions of growth have smaller surface areas, and slow growing faces, therefore, dominate the final morphology.[24,25] Lots of experimental results have demonstrated that selective adhesion of capping ligand onto specific crystal planes could control its growth rate and be critical in the epitaxial growth of nanocrystals. For nanomaterials with a hexagonal crystal structure, the surfaces are typically {0001} for top/bottom planes and a family of six energetically equivalent $\{10\bar{1}0\}$ side planes ($(10\bar{1}0)$, $(\bar{1}010)$, $(0\bar{1}10)$, $(01\bar{1}0)$, $(1\bar{1}00)$, and $(\bar{1}100)$) on the basis of the known.[26]

On the basis of the above experimental results, the effect of the NH_4F content on different aspect ratios of these $NaCeF_4$ nanorods can be explained as follows. Due to the coordination effect between F^- and Ce^{3+}, F^- inevitably capped on crystal surfaces of $NaCeF_4$ unit cell but the capping effect of F^- on the {0001} crystal planes was greater than that on the $\{10\bar{1}0\}$ planes. According to the Gibbs-Thompson theory, the relative chemical potential of a crystal is proportional to its surface−atom ratio, determined by the average number of dangling bonds per atom over the entire crystal.[27] The capping effect of F^- would decrease the average number of dangling bonds and further decrease the chemical potential of the crystal, as well as the crystal plane. When increasing NH_4F content, the surface energy of the {0001} crystal plane was decreased dramatically and, hence, the growth rate along {0001} direction was markedly decelerated because of the stronger capping effect of F^- to {0001} plane. As a result, the nanorods with smaller aspect ratio were obtained.

3.2. Effect of $NaNO_3$ Content. When the NH_4F content was fixed at 32 mmol, 2, 3, 4, 6, 8, and 10 mmol of $NaNO_3$ were applied to study the effect of $NaNO_3$ content on the crystallization and morphology. The samples with $NaNO_3$ content of 2, 4, 6, 8, and 10 mmol were specially denoted as N1, N2, N3, N4, and N5, respectively. In fact, N1 and F3 are the same sample. XRD patterns and FE-SEM images of samples N1−N5 are shown in Figure 3. XRD patterns exhibit that all of samples have a hexagonal phase and the crystallinity becomes better and better. When the $NaNO_3$ content is stoichiometric, i.e., 2 mmol, sample

dx.doi.org/10.1021/ic1022467 |*Inorg. Chem.* 2011, 50, 3387–3393

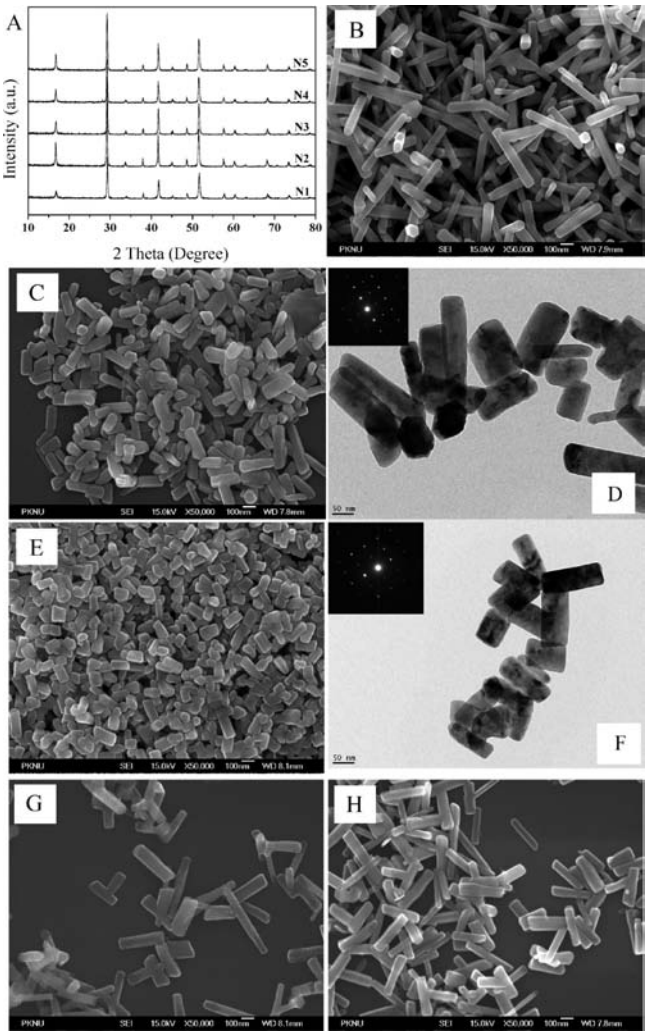

Figure 3. (A) XRD patterns of the $NaCeF_4$ samples with different $NaNO_3$ content. (B−H) FE-SEM and TEM images of corresponding $NaCeF_4$ samples. (B): N1 (2 mmol); (C, D): N2 (4 mmol); (E, F): N3 (6 mmol). G: N4 (8 mmol); H: N5 (10 mmol). The inset in the TEM images are SAED patterns from a single nanorod.

N1 exhibits uniform hexagonal nanorods with the diameter of 100 nm and length of 500 nm (Figure 3B). As the $NaNO_3$ content increases to 4 mmol, it can be seen that sample N2 is also composed of nanorods and the average diameter and length are estimated as 100 and 250 nm, respectively. However, the shape of nanorods becomes somewhat ill-regular compared with that of sample N1. The synthesis with 3 mmol $NaNO_3$ yields closely similar shape and size (see Figure S2(D), Supporting Information). When the $NaNO_3$ content increases to 6 mmol, more irregular nanorods are formed, and the length of nanorods further decreases to 150 nm. These nanorods are also highly crystalline based on the TEM and SAED examinations (see Figures 2F and 3D,F). The above shortening tendency of nanorods, however, was stopped upon further increase of $NaNO_3$ content to 8 mmol (250−300 nm) and 10 mmol (300 nm) and converted to prolonging (see Figure 3G,H). This observation indicates that stoichiometric amounts of $NaNO_3$ and heavy excess (above 4 times) favor the production of longer and more regular nanorods while keep the diameter not substantially changed. Herein, we consider that role of mineralizer of excess

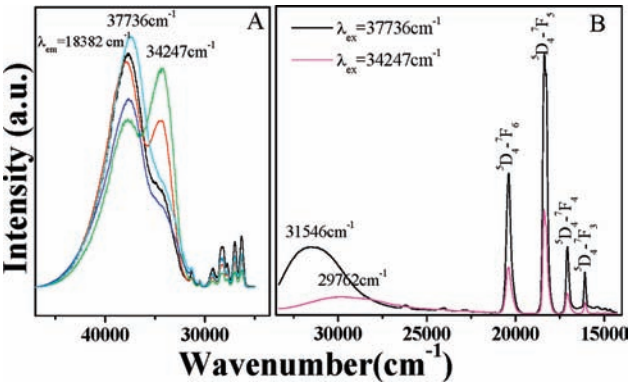

Figure 4. Excitation (A) and emission (B) spectra of $NaCeF_4:Tb^{3+}$ sample. In the excitation spectra, F2: green line; F3/N1: red line; F4: light blue line; N2: black line; N3: blue line. The representative emission spectra correspond to sample N3 with 34 247 and 37 736 cm^{-1} excitation.

$NaNO_3$ and concentration effect cowork and compete with each other in the solution system. The former increases the chemical potential of the solution and could suppresses the growth on {0001} top/bottom planes and/or facilitate the preferred increase of growth rate along $\{10\bar{1}0\}$ orientation.[24,28] While the latter works oppositely, that is, higher reactant concentration facilitates the crystal growth, because lower concentration results in fewer monomers, which usually showed size shrinkage via the well-known "defocusing" way.[29] Our results indicate that concentration effect was competitive at higher concentration and became the dominator of the nanorods growth, while mineralizer effect was much more remarkable at relatively lower concentration. As studied previously, mineralizer effects could always work in an alkali metal salts system and influence the product morphology in thermally chemical synthesis. Hexagonal LaF_3 nanoplates were synthesized using $NaNO_3$ as mineralizer, and the authors considered that regular nanoplates were formed via a dissolution−recrystallization process due to the high chemical potential caused by mineralizer $NaNO_3$.[24] With the alkali metal ion (K^+, Na^+, and Li^+)-assisted-hydrothermal method, Wang et al.[28] synthesized various bismuth ferrite compounds, and they held that alkali metal ions had pronounced influence on the solubility of Bi^{3+} and Fe^{3+} hydroxides, which led to the formation of rhombohedral $BiFeO_3$, orthorhombic $Bi_2Fe_4O_9$, and cubic $Bi_{12}(Bi_{0.5}Fe_{0.5})$-$O_{19.5}$, respectively. In this work, regular nanorods could only be obtained under suitable $NaNO_3$ content based on the competition between mineralizer and concentration effects.

3.3. Effect of Reaction Temperature. In this work, another important experimental factor, reaction temperature, was also considered to investigate the growth process of nanocrystals. Different reaction temperatures (at 120, 140, 160, 180, 200 °C) were selected to prepare the samples when the other reaction conditions were kept the same as those for the typical synthesis. It was found that the products were only CeF_3 instead of $NaCeF_4$ below 140 °C and became almost the hexagonal $NaCeF_4$ with a little CeF_3 (∼5%) at 160 °C. Pure hexagonal $NaCeF_4$ nanorods were formed as the temperature was elevated to 180 °C (see Figure S3, Supporting Information). It suggests that in this thermal system only CeF_3 can be formed in the thermodynamically stable crystalline form at low temperature and relatively high energy may be needed to overcome the dynamical energy barrier

dx.doi.org/10.1021/ic1022467 |Inorg. Chem. 2011, 50, 3387–3393

from CeF_3 to $NaCeF_4$. However, the morphology and size including the diameter and length show no change for the samples synthesized at 160, 180, and 200 °C (SEM images were not shown here). As previously demonstrated in synthesized studies of $NaYF_4$[6], reaction temperature was also a key factor in controlling the morphology and size. Different temperatures could enable the relative growth rates of various crystal facets change and finally resulted in a different aspect ratio. Generally, high temperature favors the growth of nancrystals with large particle size. However, herein the relative growth rate along the {0001} and {10$\bar{1}$0} face show no obvious change with the rise of the temperature. The aspect ratio L/D, therefore, has no obvious variation. On the basis of the above results, we could believe that $NaCeF_4$ nanorods with different aspect ratio can be obtained by controlling the reactant content.

3.4. Photoluminescence Properties. Tb^{3+} (10 mol %) doped $NaCeF_4$ hexagonal nanorods are prepared according to the typical synthesis. It should be noted that the doping with Tb^{3+} changes neither the crystalline phase nor the morphology of the matrix material. Figure 4 shows the excitation (A) and emission (B) spectra of $NaCeF_4$:Tb^{3+} nanorods with different aspect ratios. There are two different features in the UV region of the excitation spectrum (Figure 4A), where a broad and strong band originating from the allowed 4f−5d transitions of Ce^{3+} and some weak lines coming from parity-forbidden intra4f^8 transitions of Tb^{3+} ions were clearly observed as monitoring the green emission of Tb^{3+} at 18 382 cm^{-1}.[30,31] Two resolved components of Ce^{3+} in the broad excitation band, peaking at 37 736 and 34 247 cm^{-1}, should associate with the transition from the ground state $^2F_{5/2}$ of Ce^{3+} to the different components of the excited 5d levels split by the crystal field.[20] Compared with the corresponding transitions in the gaseous triply ionized Ce^{3+} (49 737 and 52 226 cm^{-1}), the ones in the solid are both red-shifted by almost the same amount (~15 000 cm^{-1}) due to the suppression of crystal field.[32,33] Given the fact that there is only one electron in the 4f configuration of the Ce^{3+} ion, which will be promoted into a 5d orbital upon the irradiation of UV photons, leaving the 4f shell empty, unlike the 4f electrons which are shielded from the ligand field by the closed 5s and 5p electron shells, the electrons occupying the 5d orbital is more sensitive as spectroscopic probe to the change of local symmetry. The excitation spectrum of Ce^{3+} can, therefore, show the direct splitting information of the 5d orbital in the crystal field.[34] Depending upon the site symmetry, the overall splitting of the 5d manifold is typically of the order of 5000−10 000 cm^{-1} when the degeneracy of the 5d state is partially or completely removed.[31] Here, the overall splitting of the 5d manifold is about 4400 cm^{-1} in terms of the observed two excitation peaks. Note that the relative intensity of two bands of Ce^{3+} ion in five samples shows some significant changes. For sample N3 with small aspect ratio, the peak at 37 736 cm^{-1} is dominant and the peak at 34 247 cm^{-1} is only a shoulder. It can be observed that the intensity of the peak at 34 247 cm^{-1} increased gradually in different samples and dominates over that at 37 736 cm^{-1} in sample F2 with higher aspect ratio. Similar spectroscopic phenomena were also observed in Ce^{3+}-ion-doped a layered structure of ammonium fluorolanthate nanocrystals upon sonication and heating, which is ascribed to the structural change caused by the removal of interlayer or connective water, giving rise to the change of crystal field strength.[31] However, in this paper, the change in the samples is the morphology (i.e., aspect ratio) rather than their crystalline structure. The intensity of lower-energy peak (at 34 247 cm^{-1}) received much more influence and exhibits the increased evolution with the increase of aspect ratio. We, therefore, can conclude that the anisotropic growth significantly modified the local symmetry surrounding the Ce^{3+} ions in $NaCeF_4$:Tb^{3+} samples. The crystal field strength applied on the Ce^{3+} ions changed and remarkably affected the sensitized luminescence routes of Tb^{3+} activators. The lower-energy level (corresponding to the peak at 34 247 cm^{-1}) of Ce^{3+} ions shows a more efficient energy transfer to Tb^{3+} ions in $NaCeF_4$:Tb^{3+} samples with higher aspect ratio, giving rise to the light emission, while it works oppositely in the samples with lower aspect ratio. Shape-dependent photoluminescence properties were previously reported by Song et al. in LaPO4:Eu^{3+} nanocrystals, where they observed the enhancement of quantum luminescent efficiency in nanowires compared with nanoparticles because of improvement of crystal anisotropy, which enhances oscillator strength.[35]

Table 1. Energy Levels of Excitation and Emission Lines (cm^{-1}) and Corresponding Assignments in Figure 4[36]

excitation spectra (Figure 4A)		emission spectra (Figure 4B)	
peaks (cm^{-1})	assignments	peaks (cm^{-1})	assignments
37736		31546	
	4f−5d (Ce^{3+})		5d−4f (Ce^{3+})
34247		29726	
31305	$^7F_6$−$^5D_0$ (Tb^{3+})	20381	$^5D_4$−$^7F_6$ (Tb^{3+})
30520	$^7F_6$−$^5D_1$(Tb^{3+})		
29205	$^7F_6$−$^5L_8$ (Tb^{3+})	18415	$^5D_4$−$^7F_5$ (Tb^{3+})
28273	$^7F_6$−$^5G_4$ (Tb^{3+})		
27762	$^7F_6$−$^5G_5$ (Tb^{3+})	17076	$^5D_4$−$^7F_4$ (Tb^{3+})
27012	$^7F_6$−$^5L_{10}$ (Tb^{3+})		
26328	$^7F_6$−$^5D_3$ (Tb^{3+})	16082	$^5D_4$−$^7F_3$ (Tb^{3+})

In Figure 4B, some strong emission lines and a weak broad band can both be observed upon excitation into the Ce^{3+} absorption band in sample N3. These green-light emitting lines should be ascribed to transitions from the excited $^5D_4$ state to the ^7F_J (J = 3−6) ground states of Tb^{3+} ions. Energy levels of excitation and emission lines (cm^{-1}) in Figure 4 and corresponding assignments are summarized in Table 1. Comparison of relative luminescence intensity of different samples was shown in Figure S4, Supporting Information; excitation and emission spectra of lower concentration of Tb^{3+} at 1% were shown in Figure S5, Supporting Information. This result indicates that an efficient energy transfer process from Ce^{3+} to Tb^{3+} occurs in $NaCeF_4$:Tb^{3+} samples.[20] That is, the Ce^{3+} acted as a sensitizer to absorb UV light and then transfer the energy to Tb^{3+}, allowing the particles to emit green fluorescence. The broad band in the 33 000 to 25 000 cm^{-1} range should be assigned to the parity-allowed transitions of the lowest component of the 2D state to the spin−orbit components of the ground, such as $^2F_{5/2,7/2}$ of the Ce^{3+} ion. The presence of the Ce^{3+} emission band suggests that the energy transfer from Ce^{3+} to Tb^{3+} is incomplete. Note that the position of emission of Ce^{3+} varied upon excitation into different levels of the 5d state of Ce^{3+}. Upon 37 736 cm^{-1} excitation, the emission of Ce^{3+} was centered at 31 546 cm^{-1} while, upon 34 247 cm^{-1} excitation, it was centered at 29 726 cm^{-1} instead. This result supports the crystal-anisotropy modified crystal field around Ce^{3+} ions. The room-temperature luminescent dynamics were also measured. Figure 5 shows the

dx.doi.org/10.1021/ic1022467 |Inorg. Chem. 2011, 50, 3387–3393

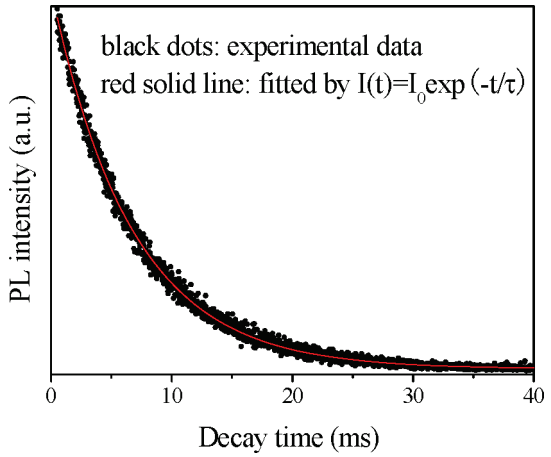

Figure 5. Luminescence decay curve at 18 382 cm^{-1} from $^5D_4$ energy level of Tb^{3+} under 40 816 cm^{-1} excitation in sample F2.

luminescent decay curves of sample F2 by monitoring the emission of Tb^{3+} at 544 nm. It can be seen that the curves can be well fitted with a single-exponential function. The lifetime is determined to be 6.75 ± 0.02 ms. Generally, the luminescence lifetime of the $^5D_4$ level is on the order of millisecond magnitude. The above observation is in good accordance with previous report.[33] The lifetimes of samples F3 (6.87 ± 0.11 ms), F4 (6.64 ± 0.03 ms), N2 (6.62 ± 0.02 ms), and N3 (7.10 ± 0.15 ms) were also examined and exhibited no appreciable variation compared with that of sample F2. The above results indicated that the intra4f[8] luminescence of Tb^{3+} does not suffer from significant influence by anisotropic shape.

4. CONCLUSIONS

In summary, monodisperse hexagonal $NaCeF_4$ and $NaCeF_4$:Tb^{3+} nanorods with controlled aspect ratios have been successfully synthesized. Various spectroscopic techniques such as XRD, SEM, TEM, PL, and a dynamic process were employed to examine their phase, size, morphology, and luminescence properties. The content of NH_4F and $NaNO_3$ plays a critical role in controlling the final morphology and size of the product. The higher the NH_4F or slight excess $NaNO_3$ content, the smaller was the obtained aspect ratio. PL spectra of $NaCeF_4$:Tb^{3+} samples exhibited characteristic emissions of Ce^{3+} (5d−4f) and Tb^{3+} (f−f), respectively. More importantly, shaped-anisotropy modified luminescence routes from Ce^{3+} to Tb^{3+} were observed in different $NaCeF_4$:Tb^{3+} samples. The relative intensity of two different excitation components (located at 37 736 and 34 247 cm^{-1}) of the Ce^{3+} 5d states as monitoring the Tb^{3+} emission varied due to the changed local crystal-field environment induced by anisotropic growth. The lower-energy level (corresponding to peak at 34 247 cm^{-1}) shows a more efficient energy transfer to Tb^{3+} ions in $NaCeF_4$:Tb^{3+} samples with higher aspect ratio, while it works oppositely in the samples with lower aspect ratio. In contrast, the intra4f[8] luminescence of Tb^{3+} shows no significant shape dependence.

■ ASSOCIATED CONTENT

Supporting Information. XRD patterns of samples synthesized with different NH_4F content: (A) 16 mmol; (B) 18 mmol; (C) 20 mmol; (D) 28 mmol; (E) 60 mmol (Figure S1); FE-SEM images of samples synthesized using: (A, B) 2 mmol $Ce(NO_3)_3$, 2 mmol $NaNO_3$, 60 mmol NH_4F; (C) 2 mmol $Ce(NO_3)_3$, 2 mmol $NaNO_3$, 28 mmol NH_4F; (D) 2 mmol $Ce(NO_3)_3$, 3 mmol $NaNO_3$, 32 mmol NH_4F (Figure S2); XRD patterns of samples synthesized at different temperature (2 mmol $Ce(NO_3)_3$, 2 mmol $NaNO_3$, 32 mmol NH_4F) (Figure S3); Comparison of emission intensity of different samples (F2, F3/N1, F4, N2, N3) (Figure S4); Excitation and emission spectra of $NaCeF_4$: Tb^{3+}(1 mol %) sample (Figure S5). This material is available free of charge via the Internet at http://pubs.acs.org.

■ AUTHOR INFORMATION

Corresponding Author

*E-mail: jhjeong@pknu.ac.kr. Tel: +82-51-629-5564. Fax: +82-51-629-5549.

■ ACKNOWLEDGMENT

This work was supported by the National Research Foundation of Korea (NRF) grant funded by the Korean government (MEST) (No. 2010-0029885), and also, this research was supported by NCRC (National Core Research Center) program through the National Research Foundation of Korea funded by the Ministry of Education, Science, and Technology (2010-0001-226).

■ REFERENCES

(1) Stouwdam, J. W.; van Veggel, F. C. J. M. *Nano Lett.* **2002**, *2*, 733–737.
(2) Yi, G. S.; Lu, H. C.; Zhao, S. Y.; Yue, G.; Yang, W. J.; Chen, D. P.; Guo, L. H. *Nano Lett.* **2004**, *4*, 2191–2196.
(3) Sivakumar, S.; van Veggel, F. C. J. M.; Raudsepp, M. *J. Am. Chem. Soc.* **2005**, *127*, 12464–12465.
(4) Burda, C.; Chen, X.; Narayanan, R.; El-Sayed, M. A. *Chem. Rev.* **2005**, *105*, 1025–1102.
(5) Rahman, P.; Green, M. *Nanoscale* **2009**, *1*, 214–224.
(6) Li, C.; Zhang, C.; Hou, Z.; Wang, L.; Quan, Z.; Lian, H.; Lin, J. *J. Phys. Chem. C* **2009**, *113*, 2332–2339.
(7) Miao, Z. J.; Liu, Z. M.; Ding, K. L.; Han, B. X.; Miao, S. D.; An, G. M. *Nanotechnology* **2007**, *18*, 125605.
(8) Downing, E.; Hesselink, L.; Ralston, J.; Macfarlane, R. *Science* **1996**, *273*, 1185–1189.
(9) Wegh, R. T.; Donker, H.; Oskam, K. D.; Meijerink, A. *Science* **1999**, *283*, 663–666.
(10) Zhuang, J.; Liang, L.; Sung, H. H. Y.; Yang, X.; Wu, M.; Williams, I. D.; Feng, S.; Su, Q. *Inorg. Chem.* **2007**, *46*, 5404–5410.
(11) Zhang, F.; Li, J.; Shan, J.; Xu, L.; Zhao, D. *Chem.—Eur. J.* **2009**, *15*, 11010–11019.
(12) Wang, X.; Li, Y. *Chem.—Eur. J.* **2003**, *9*, 5627–5635.
(13) Wang, X.; Zhuang, J.; Peng, Q.; Li, Y. *Inorg. Chem.* **2006**, *45*, 6661–6665.
(14) Li, S.; Xie, T.; Peng, Q.; Li, Y. *Chem.—Eur. J.* **2009**, *15*, 2512–2517.
(15) Mai, H.; Zhang, Y.; Si, R.; Yan, Z.; Sun, L.; You, L.; Yan, C. *J. Am. Chem. Soc.* **2006**, *128*, 6426–6436.
(16) Wei, Y.; Lu, F.; Zhang, X.; Chen, D. *Chem. Mater.* **2006**, *18*, 5733–5737.
(17) Zeng, J. H.; Li, Z. H.; Su, J.; Wang, L.; Yan, R.; Li, Y. *Nanotechnology* **2006**, *17*, 3549–3555.
(18) Liu, C.; Wang, H.; Zhang, X.; Chen, D. *J. Mater. Chem.* **2009**, *19*, 489–496.
(19) Laudise, R. A.; Ballman, A. A. *J. Phys. Chem.* **1960**, *64*, 688–691.
(20) Li, C. X.; Yang, J.; Quan, Z. W.; Yang, P. P.; Kong, D. Y.; Lin., J. *Chem. Mater.* **2007**, *19*, 4933–4942.

(21) W. Krämer, K.; Biner, D.; Frei, G.; U. Güdel, H.; P. Hehlen, M.; Lüthi S, R. *Chem. Mater.* **2004**, *16*, 1244–1251.
(22) Wang, F.; Han, Y.; Lim, C. S.; Lu, Y.; Wang, J.; Xu, J.; Chen, H.; Zhang, C.; Hong, M.; Liu, X. *Nature* **2010**, *463*, 1061–1065.
(23) Shannon, R. D. *Acta Crystallogr. A* **1976**, *32*, 751–767.
(24) Qin, R.; Song, H.; Pan, G.; Bai, X.; Dong, B.; Xie, S.; Liu, L.; Dai, Q.; Qu, X.; Ren, X.; Zhao., H. *Cryst. Growth Des.* **2009**, *9*, 1750–1756.
(25) Yang, J.; Li, C. X.; Quan, Z. W.; Kong, D. Y.; Zhang, X. M.; Yang, P. P.; Lin, J. *Cryst. Growth Des.* **2008**, *8*, 695–699.
(26) Li, C. X.; Quan, Z. W.; Yang, J.; Yang, P. P.; Lin, J. *Inorg. Chem.* **2007**, *46*, 6329–6337.
(27) Yu, S. H.; Liu, B.; Mo, M. S.; Huang, J. H.; Liu, X. M.; Qian, Y. T. *Adv. Funct. Mater.* **2003**, *13*, 639–647.
(28) Wang, Y. G.; Xu, G.; Yang, L. L.; Ren, Z. H.; Wei, X.; Weng, W. J.; Du, P. Y.; Shen, G.; Han, G. R. *J. Am. Ceram. Soc.* **2007**, *90*, 3673–3675.
(29) Peng, X.; Manna, L.; Yang, W.; Wickham, J.; Scher, E.; Kadavanich, A.; Alivisatos, A. P. *Nature* **2000**, *404*, 59–61.
(30) Di, W.; Willinger, M. G.; A. S. Ferreira, R.; Ren, X.; Lu, S.; Pinna, N. *J. Phys. Chem. C* **2008**, *112*, 18815–18820.
(31) Ghosh, P.; Kar, A.; Patra, A. *J. Phys. Chem. C* **2010**, *114*, 715–722.
(32) Dorenbos, P. *Phys. Rev. B* **2000**, *62*, 15640–15649.
(33) Lang, R. J. *Can. J. Res.* **1936**, *14*, 127–130.
(34) Lai, H.; Bao, A.; Yang, Y.; Tao, Y.; Yang, H.; Zhang, Y.; Han, L. *J. Phys. Chem. C* **2008**, *112*, 282–286.
(35) Song, H.; Yu, L.; Lu, S.; Wang, T.; Liu, Z.; Yang, L. *Appl. Phys. Lett.* **2004**, *85*, 470.
(36) Carnall, W. T.; Fields, P. R.; Rajnak, K. *J. Chem. Phys.* **1968**, *49*, 4447–4449.